JOURNAL OF GEOPHYSICAL RESEARCH, VOL. 113, B05402, doi:10.1029/2007JB004962, 2008

Relating permeability to the structural setting of a fault-controlled hydrothermal system in southeast Oregon, USA

Todd R. Anderson[1] and Jerry P. Fairley[2]

Received 30 January 2007; revised 4 December 2007; accepted 18 January 2008; published 6 May 2008.

[1] It is generally accepted that high-permeability pathways are required to bring hydrothermal fluids to the surface from depth at elevated temperatures, and these pathways are commonly associated with faulting. The orientation and mode of fractures that develop as a result of fault slip are dependent on the state of stress and the geometry of the fault system, which in turn control the near-fault permeability structure. We hypothesize that temperature data collected in fault-controlled hydrothermal systems may be used to delineate the extent of the near-surface breakdown region of the controlling fault, and may provide insight regarding the fault geometry and stress field. Here we present a geostatistical analysis of 1550 ground and spring temperature measurements in an area of active hydrothermal discharge located at Mickey Hot Springs in southeast Oregon. Indicator kriging was used to treat heterogeneity across the site prior to in-category simulation of temperature as a continuous variable. The analysis indicates that zones of high, medium, and low temperature at the site arise from different physical mechanisms, which we propose are related to the underlying modes of fracturing and the dominant mechanisms of heat and mass transport (i.e., by advection or diffusion). The findings of this study suggest that thermal-hydrologic data of the type presented here may be useful for understanding fault zone characteristics, and for developing conceptual models of fault-controlled fluid flow.

Citation: Anderson, T. R., and J. P. Fairley (2008), Relating permeability to the structural setting of a fault-controlled hydrothermal system in southeast Oregon, USA, *J. Geophys. Res.*, *113*, B05402, doi:10.1029/2007JB004962.

1. Introduction

[2] Fault zones are highly heterogeneous structures characterized by distinct architectural elements. These elements are generally divided into three main categories: the highly deformed fault core, which accommodates the majority of slip across the fault; the surrounding, undeformed protolith [*Chester and Logan*, 1986; *Caine et al.*, 1996]; and the damage zone(s), which are transitional regions between the core and the protolith. Faults may form conduits to subsurface fluid flow, barriers to flow, or combinations of conduits and barriers, and their properties may evolve over time [*Caine et al.*, 1996; *Davatzes et al.*, 2005].

[3] Hot springs are commonly found in areas of active faulting [*Barton et al.*, 1995; *Curewitz and Karson*, 1997; *Micklethwaite and Cox*, 2004; *Norton and Knapp*, 1977]. High-permeability pathways are required to bring hydrothermal fluids from depth to the land surface [*Forster and Smith*, 1988]; the low bulk permeability of non-fractured rock suggests that faults are likely to form conduits for hydrothermal fluids, and explains the association between hot springs and active faulting. However, as hydrothermal fluids migrate from depth they cool and degas, and significant mineral precipitation may be expected to reduce permeability and ultimately block discharge in the absence of any physical mechanism of permeability maintenance [*Bishop and Bird*, 1987; *Davatzes and Hickman*, 2005; *Elders et al.*, 1984; *Hickman et al.*, 1998; *Micklethwaite and Cox*, 2004; *Sibson*, 1987]. One conceptual model associates hot spring development with either the maintenance of existing permeability or the creation of new permeable pathways, and divides the structural settings of hydrothermal springs into two broad categories (with six sub-categories) on the basis of this distinction [*Curewitz and Karson*, 1997]. In both of these cases (maintenance of existing permeability versus creation of new permeability) permeability is maintained by stress concentration, although the mechanisms that accommodate the deformation of fault slip are different.

[4] Previous investigations have used geostatistical analyses of hot spring and ground temperatures to develop models for the distribution of permeability in the Borax Lake fault, an active Basin and Range normal fault located in southeast Oregon [*Fairley et al.*, 2003; *Fairley and Hinds*, 2004; *Heffner and Fairley*, 2006]. While those analyses provided information on the distribution of permeability within the fault controlling hydrothermal dis-

[1]Environmental Science Program, University of Idaho, Moscow, Idaho, USA.
[2]Department of Geological Sciences, University of Idaho, Moscow, Idaho, USA.

0148-0227/08/2007JB004962$09.00

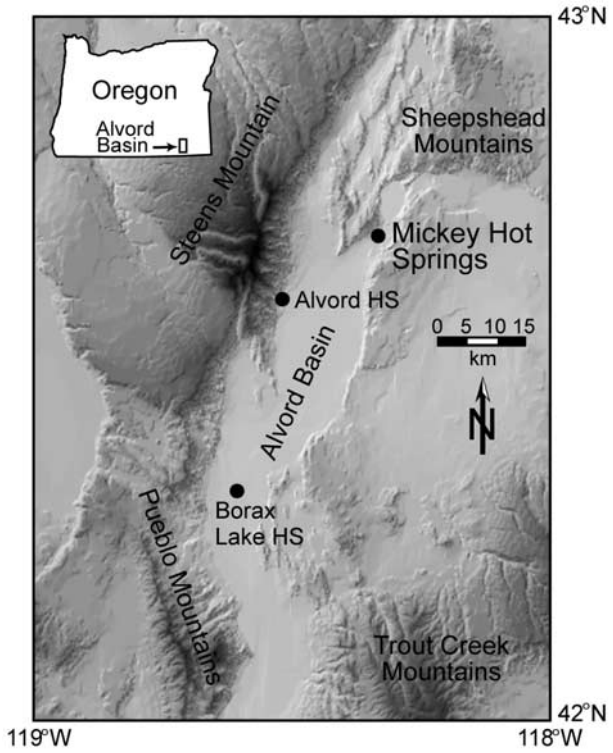

Figure 1. Shaded relief map, showing the location of the study area at Mickey Hot Springs, located in the Alvord Basin, southeast Oregon, USA. Reprinted from *Heffner and Fairley* [2006] with permission from Elsevier.

charge at the site, a worldwide survey of more than 800 hot springs found that the only about 6% of all hydrothermal springs are distributed along the trace of a controlling fault (the setting of the Borax Lake hot springs), whereas approximately 29% of hydrothermal activity occurs either at the tip-lines of single faults or in the interaction area between two fault tips [*Curewitz and Karson*, 1997]. As a first step toward applying the methods developed in the Borax Lake system to a wider variety of structural settings, we present here a geostatistical analysis of temperature measurements made within the Mickey Hot Springs area in the Alvord Basin of southeast Oregon. In this study, we use indicator transforms to separate the measured temperatures into domains based on their spatial characteristics, and treat each domain as arising from a different generating process in subsequent continuous-variable simulations. This approach allows a more accurate representation of temperature distributions in the model domain, and provides insight into the distribution of heterogeneity at the Mickey Hot Springs site. Heterogeneity is of particular importance and influence in flow simulations [*Eaton*, 2006], and is often the most consequential feature of numerical simulations [*Deutsch and Journel*, 1998]. Indicator coding separates the property of interest (in this case, temperature) into exclusive domains prior to simulating the variable of interest within each category [*Koltermann and Gorelick*, 1996; *Rubin*, 2003], and may be useful in attaching physical significance to different generating processes. Following previous investigators [e.g., *Fairley and Hinds*, 2004; *Heffner and Fairley*, 2006], temperature is treated as a proxy for permeability due to increased advective heat transport in areas of increased fracturing. Finally, we present some brief comments regarding the structural settings that could give rise to the distribution of temperature/permeability observed at the site and discuss possible applications of thermal data to the study of fault hydrologic architecture.

2. Geologic Setting

[5] The study area is located in the Alvord Basin of southeast Oregon (Figure 1), in the northern part of the Basin and Range Province. Horst and graben features are characteristic of the province due to east-west extension, and the Alvord Basin forms a complex north-south trending graben, bounded on the west by the Steens Mountain and Pueblo Mountains horst blocks, and on the east by the topographically lower Trout Creek Mountains horst block. The stratigraphic sequence of crystalline rocks that forms the basement complex is exposed along the basin-bounding Steens and Alvord faults on the western margin of the basin, comprising primarily volcanic or volcaniclastic rocks, including rhyolites, tuffs, and andesitic and basaltic lava flows that exceed 2500 m in total thickness. This sequence includes the Alvord Creek Formation, Pike Creek Volcanics, Steens Mountain Volcanics, and the Steens Mountain Basalt [*Fuller*, 1931; *Williams and Compton*, 1953]. Geologic maps of the area [*Minor et al.*, 1987; *Rytuba et al.*, 1982; *Sherrod et al.*, 1989; *Walker and Repenning*, 1965] give more detailed descriptions of the stratigraphic sequence, and provide additional information on faults within and around the basin. Numerous north-northeast trending normal faults are found in the area due to regional extension and the basin is subject to dextral shearing [*Pezzopane and Weldon*, 1993] giving rise to strike-slip faults [*Lawrence*, 1976], some of which link the north-northeast trending normal faults [*Williams and Compton*, 1953].

[6] Three main groups of thermal springs discharge within the Alvord Basin. Borax Lake Hot Springs are located near the center of the valley, along the trace of an en echelon normal fault [*Fairley et al.*, 2003]. Both Alvord and Mickey Hot Springs discharge from range-front faults. Alvord Hot Springs occur near the base of Steens Mountain along the western margin of the basin, while Mickey Hot Springs are at the base of Mickey Butte, on the opposite side of the valley from Alvord Hot Springs and further north. The geothermal system within the Alvord Basin has been described by several authors, including *Brown and Peterson* [1980], *Cleary* [1974], and *Cummings et al.* [1993]. Oxygen and hydrogen isotope analysis suggests that thermal waters within the valley are of meteoric origin [*Cleary*, 1974; *Cummings et al.*, 1993; *Koski and Wood*, 2004], with recharge areas being topographic highs near the hot springs. Chemical and isotopic geothermometers indicate reservoir temperatures around 200°C [*Cummings et al.*, 1993; *Koski and Wood*, 2004]. *Cummings et al.* [1993] used stratigraphic reconstructions in conjunction with strontium isotope data to estimate depths of circulation of 1.2 – 2.0 km for Mickey Hot Springs, 2.0 – 2.5 km for Borax Lake Hot Springs, and 2.0 – 3.0 km for Alvord Hot Springs. The heat source for the hydrothermal areas in the basin is

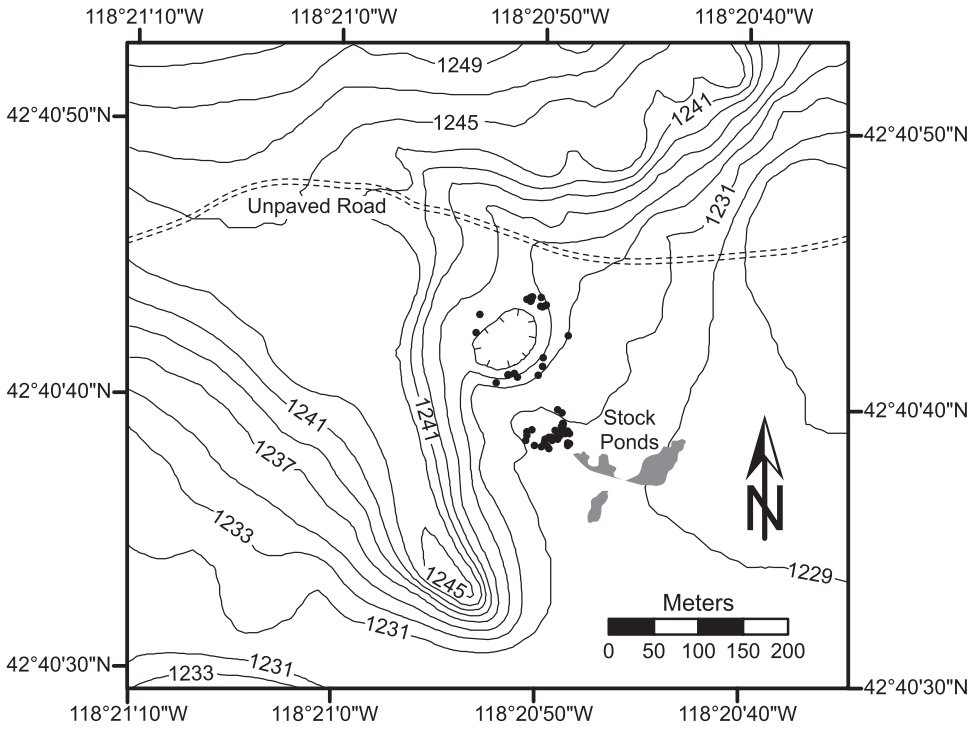

Figure 2. Topographic map of the Mickey Hot Springs study area. The filled-in circles represent the locations of individual hot spring vents. The area shown in this figure is a sub-domain of Figure 3. Contour interval is 2 m.

uncertain, but published evidence does not currently favor a magmatic component [*Cleary*, 1974; *Koski and Wood*, 2004].

[7] The site of the present investigation is Mickey Hot Springs (Figure 2). The study site is underlain by Miocene volcanic rocks, primarily the Steens Basalt [*Sherrod et al.*, 1989; *Walker and MacLeod*, 1991; *Walker and Repenning*, 1965]. *Hook* [1981] describes two additional volcanic units in the Mickey area that overlay the Steens Basalt: a layer of rhyolite ignimbrite (Mickey Ignimbrite), overlain in turn by a series of basalt lava flows (Mickey Basalt). The hot springs are found within the Mickey Basin, a northeast-striking graben in the northeastern arm of the Alvord Desert. Major range-front faults in the area define the graben, with fault scarps in late Pleistocene and Holocene alluvial and lacustrine deposits apparent along the northwest and southeast range front margins; these deposits are associated with pluvial lakes in the Alvord Basin [*Lindberg*, 1999]. Faults in the area are mapped as normal or high-angle faults with a southeast or northwest direction of dip [*Brown and Peterson*, 1980; *Hook*, 1981; *Walker and MacLeod*, 1991; *Walker and Repenning*, 1965; *Weldon et al.*, 2003]. *Weldon et al.* [2003] indicate activity along the range-front faults within the last 10,000 years, while *Lindberg* [1999] estimates an age of 2000 years for the youngest event on the fault that forms the range front to the north of the Mickey Hot Springs. *Hook* [1981] shows an intrabasin northeast-trending normal fault controlling the location of Mickey Hot Springs, but presented no additional detail regarding the geometry of the proposed fault (e.g., dip angle or direction). J.S. Oldow [unpublished data, 2006] mapped additional intrabasin northeast-southwest striking normal faults in Mickey Basin, including two segments that capture the group of hot springs, placing the springs within a fault-tip interaction zone (Figure 3).

3. Data Collection

[8] The initial reconnaissance of the Mickey Hot Springs area took place in March 2003. 57 geothermal springs were identified and mapped using dual-frequency, radio-linked Lecia global positioning system receivers with an accuracy estimated to be better than one meter (horizontal). Additional fieldwork included a survey of spring temperatures and site characterization such as digital photographs and written descriptions of spring characteristics (e.g., shape, size, vegetation, geology). The data set used in the present study consists of 1550 temperature measurements taken within a 55 $\times$ 36 m area of the southern, more active portion of Mickey Hot Springs. The data were collected over a one-day period during May 2004 to minimize the influence of diurnal temperature fluctuations. Ground temperatures were measured on a 1 $\times$ 1 m grid spacing within the study area; temperatures were measured using DIGI-SENSE Type K Penetration (4 inch) thermocouple probes in conjunction with FLUKE 51 digital thermometers. Spring temperatures used in the analysis are based on three to five individual measurements per spring, taken as close to the vents as possible to minimize thermal mixing effects. In the analysis that follows, ground temperature measurements are assumed to be in approximate equilibrium with shallow ($\sim$0.1 m) subsurface fluids, as is customary in problems of

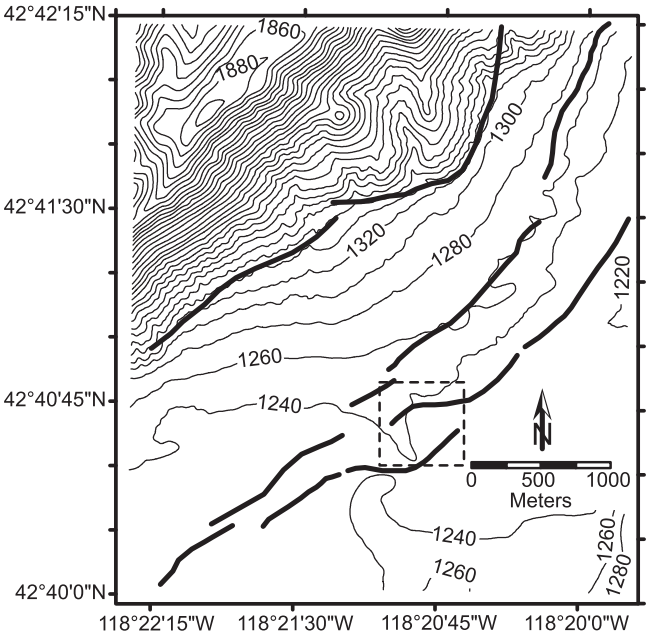

Figure 3. Topographic map of the study area and surroundings. The heavy lines indicate the positions of faults mapped in the field by J.S. Oldow [unpublished data, 2006]. The approximate area of the map shown in Figure 2 is indicated by the dotted line. Contour interval is 20 m.

heat and mass transport in porous media [e.g., *Catton*, 1985; *Cheng*, 1985; *Wong and Dybbs*, 1976].

4. Geostatistical Analysis and Results

[9] The goal of any geostatistical analysis is to explain how a variable fluctuates in space or time using predictive statistics to characterize any unsampled value [*Deutsch and Journel*, 1998]. A tool commonly used to quantitatively describe spatial variability is the experimental variogram, defined mathematically as:

$$\gamma(h) = \frac{1}{2N(h)} \sum (z_i - z_{i+h})^2$$

where h is the separation or lag distance between data values z_i and z_{i+h}, and $N(h)$ is the number of data pairs that are separated by the distance h [*Deutsch and Journel*, 1998; *Goovaerts*, 1997; *Isaaks and Srivastava*, 1989]. The experimental variogram is fitted with a model or linear combination of models such that a variogram value for any separation distance can be computed. The resulting variogram model can be used in a variety of ways to make estimates of unknown values at specific locations. Kriging is an estimation method that uses linear regression techniques to make estimates based on neighboring data values. The aim of kriging is to minimize the estimation error variance. Because kriging is an interpolator, it tends to overestimate small values and underestimate large values, resulting in a smoothed representation of spatial variability [*Goovaerts*, 1997]. Image simulation is an alternative to estimation. Simulation aims to reproduce the spatial distribution pattern and statistics of the sampled data. Simulation is not an interpolator, but rather allows for the presence of extreme values and their pattern of continuity [*Rubin*, 2003].

[10] Large-scale heterogeneities are known to be consequential features of numerical models [*Deutsch and Journel*, 1998]. Unfortunately, models based on a continuous variable cannot reproduce severe heterogeneities or boundaries, necessitating additional steps in a geostatistical analysis if such heterogeneities are present and important. The geometry or spatial architecture of the major domains should be modeled and reproduced first using "categorical" variables, followed by simulation of the population within each domain. Situations such as this often benefit from an indicator approach: geometry is modeled and reproduced through the use of indicator transforms of the categorical variable type defined as [*Deutsch and Journel*, 1998]:

$$ind_i = \begin{cases} 1, & if \;\; x_i = s_k \\ 0, & otherwise \end{cases}$$

where x_i is the data value and s_k is the category. This requires the specification of a categorical variable and category to create the indicator transform. A similar method could utilize indicator transforms of the continuous variable type defined as [*Deutsch and Journel*, 1998]:

$$ind_i = \begin{cases} 1, & if \;\; x_i \le cut_k \\ 0, & otherwise \end{cases}$$

where x_i is the data value and cut_k is the cutoff or threshold value specified by the investigator. Experimental indicator variograms are calculated using the indicator transformed values for each category or cutoff, depending on the variable type. Each experimental indicator variogram is then modeled and the collection of models used in indicator kriging or simulation [e.g., *Goovaerts et al.*, 1997; *Journel and Alabert*, 1990; *Journel and Isaaks*, 1984; *Suro-Perez and Journel*, 1990]. An indicator approach also avoids stretching the assumption of stationarity [*Deutsch and Journel*, 1998; *Isaaks and Srivastava*, 1989].

[11] The indicator approach was used in this study to delineate temperature domains within the study area. Experimental indicator variograms of the continuous variable (temperature) were computed using routines in the software suite GSLIB [*Deutsch and Journel*, 1998]. Nine isotropic variograms were computed using the entire sample data set; the nine decile temperature values were utilized as cutoffs in the indicator transforms. On the basis of these nine experimental indicator variograms, it was determined that there were three distinct domains represented within the data. Additional experimental indicator variograms were computed with cutoffs in the ranges of 24.9 – 27.7°C and 49.3 – 60.9°C, to investigate the temperature ranges in which the variograms appeared to change shape. It was determined that the cutoffs to divide the study area into different temperature domains would be set at 27.2 and 58.1°C; that is, any temperature measurement less than or equal to 27.2°C would be treated separately from any temperature that was greater than 27.2°C but less than or equal to 58.1°C, and any temperature measurement greater than 58.1°C would be treated separately from those that fell

Table 1. Indicator Variogram Model Parameters

Domain Direction	Structure	Nugget	Sill Contribution	Range
Low	exponential	0.02	0.030	6
70°	exponential		0.060	10
Low	exponential	0.02	0.020	4
160°	exponential		0.080	9
Medium	exponential	0.05	0.125	6
Isotropic	exponential		0.075	30
High	exponential	0.06	0.040	7
30°	exponential		0.120	30
High	exponential	0.06	0.042	5
120°	exponential		0.052	10

into either of the other two domains. The first domain, with temperatures less than or equal to 27.2°C, was called the low temperature domain; the second domain, with temperatures greater than 27.2 but less than or equal to 58.1°C, was called the medium temperature domain, and the third domain, with temperatures greater than 58.1°C, was referred to as the high temperature domain.

[12] Once the temperature domains were delineated, their geometry could be modeled. Before experimental indicator variograms were computed, variogram maps were constructed to aid in the detection of anisotropy. A variogram map is a plot of experimental variogram values in all directions and at many lags. The center of the map corresponds to the origin of the experimental variogram; variogram values near the origin represent small separation distances (lags) between pairs of data points, and lags increase with increasing distance away from the origin. If anisotropy is not present, the increase in variogram values away from the origin is similar in all directions, resulting in a circular pattern; conversely, anisotropy becomes apparent when the increase of variogram values is not uniform in all directions, resulting in an elliptical pattern [*Goovaerts*, 1997; *Isaaks and Srivastava*, 1989]. The direction in which variogram values increase more slowly (along the major axis of the ellipse) is the direction of maximum continuity. Variogram maps were generated using the appropriate GSLIB [*Deutsch and Journel*, 1998] routines. Three maps were generated using indicator variograms (i.e., categorical variables), one each for the high, medium, and low categorical inputs. The variogram maps for the low and high temperature domains suggested a possible anisotropy in a northeast-southwest direction, while the variogram map for the medium temperature domain did not suggest an apparent anisotropy. Plots of the indicator transforms (i.e., indicator maps) for each of the domains were generated and used to verify the spatial continuity suggested by the variogram maps. Experimental indicator variograms of the categorical variable type for each of the domains were computed and plotted as a guide to choosing the orientations of maximum and minimum continuity. Directions chosen for the experimental variograms in the low temperature domain were 70° and 160°, corresponding to the major and minor ranges, respectively; directions chosen for the experimental variograms in the high temperature domain were 30° and 120°, also corresponding to the respective major and minor ranges. The experimental variogram for the medium temperature domain was modeled as isotropic.

[13] The experimental indicator variograms were modeled to obtain continuous representations of the data, and the fit of each model to its corresponding experimental indicator variogram was fine-tuned using a sum of squares criterion that minimized the sum of the differences between the predicted model values and the experimental values over an appropriate range [*Cressie*, 1985]. Of the standard variogram models (i.e., models that satisfy the required positive definite condition), we found that exponential models best represented the experimental variograms describing the observed spatial variability. An exponential model is defined mathematically as [*Deutsch and Journel*, 1998]:

$$\gamma(h) = c \cdot \left[1 - \exp\left(\frac{-3h}{a}\right)\right]$$

where a is the effective range (in the case of the exponential model the range is defined as the separation distance at which the variogram reaches 95% of maximum) and c is the positive variance contribution, or contribution to the sill. Each experimental indicator variogram was modeled with nested exponential models (two exponential models with different contributions to the range and sill); model parameters are given in Table 1. Figure 4 shows each experimental variogram and its corresponding model variogram. The objective of variogram modeling is to capture the major spatial features of the attribute being modeled, rather than simply fitting the data to an arbitrary precision [*Goovaerts*, 1997]. In this study, short range correlations are thought to be more important than long range correlation due to the density of the measured data points; therefore, care was taken to fit the models more accurately at short lag distances. Figure 4b shows an experimental variogram that was modeled with a parsimonious combination of nested structures that captured the short range features, rather than an unjustifiably complicated set of nested structures used to fit the data at longer, but arguably less important, lag distances.

[14] Cross-validation was used to check the models' ability to estimate the data correctly [*Davis*, 1987]. In cross-validation, each data value is removed, one at a time, and the value at this location is estimated using the variogram model and neighboring data as conditioning points. The models used in this study were cross-validated and the residuals were analyzed and checked against the criteria put forth by *Kitanidis* [1997], which require a number of statistical tests, including normally distributed and uncorrelated residuals. The validated indicator variogram models were input to an indicator kriging (IK) routine; IK is an exact interpolator, meaning it honors indicator data at known (measured) locations. Estimates were made on a 0.25 × 0.25 m grid within the study area; Figure 5 shows a map of the IK results, in which the study area has been divided into domains of low, medium, and high temperature.

[15] The final step in the present geostatistical analysis was the simulation of in-category temperatures for each of the temperature domains estimated by IK. Stochastic simulation is the process of building alternative, equally probable, high-resolution realizations of the spatial distribution of a variable [*Deutsch and Journel*, 1998]. Many simulation methods and algorithms exist [see *Deutsch and Journel*, 1998; *Goovaerts*, 1997; *Rubin* 2003]; sequential Gaussian simulation was chosen for the present study because of its

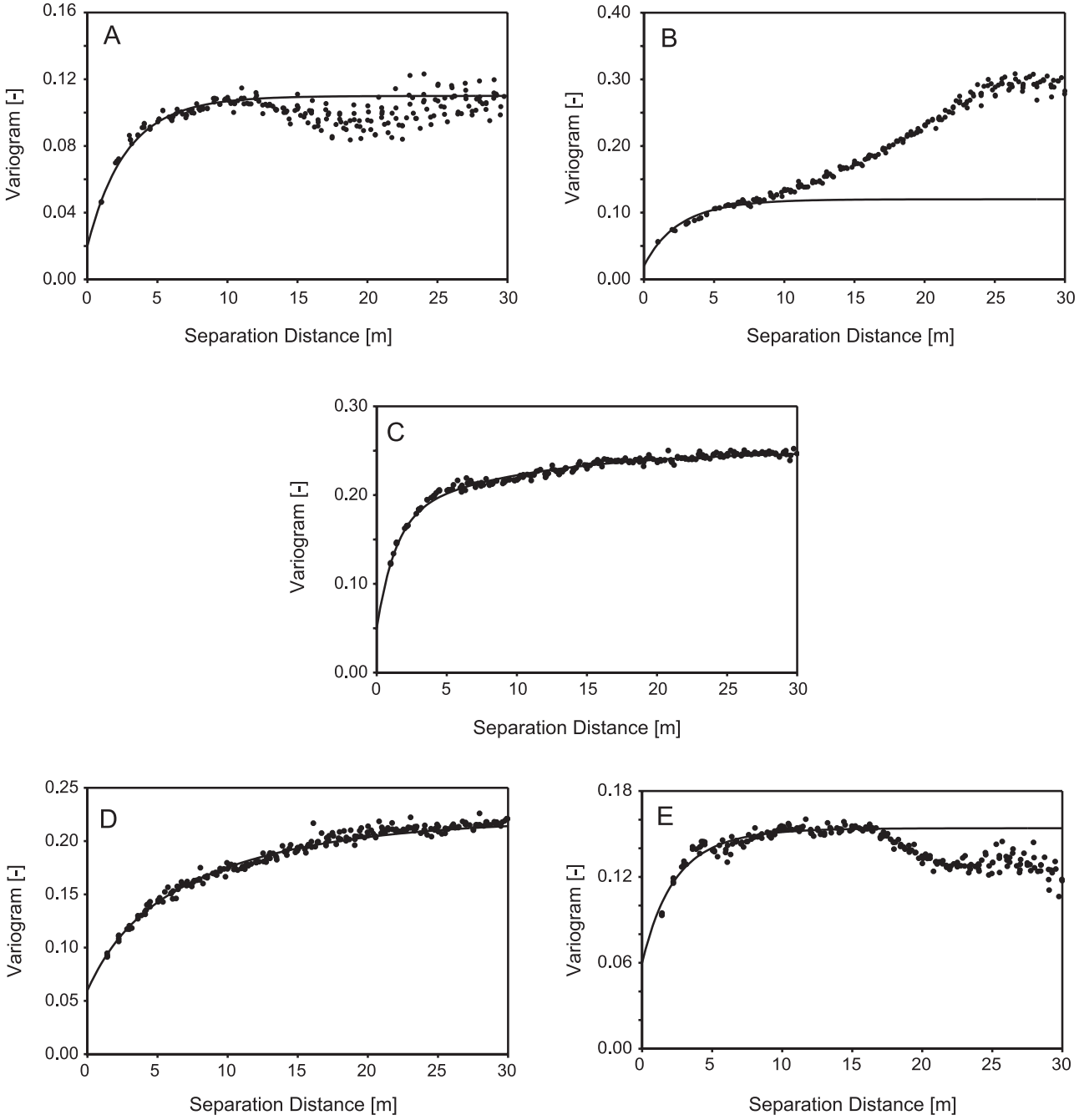

Figure 4. Variograms used for indicator kriging. Points represent experimental variogram values, solid lines are the model variograms fit to the data using the parameters given in Table 1. (a) Anisotropic variogram for the low temperature domain, oriented at 70°; (b) Anisotropic variogram for the low temperature domain, oriented at 160°; (c) Isotropic variogram for the medium temperature domain; (d) Anisotropic variogram for the high temperature domain, oriented at 30°; (e) Anisotropic variogram for the high temperature domain, oriented at 120°.

robust character and established record of successful applications when dealing with continuous spatial phenomena. The approach is considered "sequential" because simulated values are conditioned not only on sampled data within the search neighborhood, but also on approximated values already drawn (simulated) at unsampled locations. Gaussian-related algorithms require a variable that is multivariate normal. A necessary step in meeting the requirement of multivariate normality is the transformation of the data to normal scores; the continuous temperature data within each domain were transformed separately so that the distribution of temperatures within each domain was normalized. The new variable, normal score temperature, is univariate normal. Subsequently, the data were checked for bivariate normality by creating p-quantile indicator variograms and checking for symmetric destructuration; that is, checking

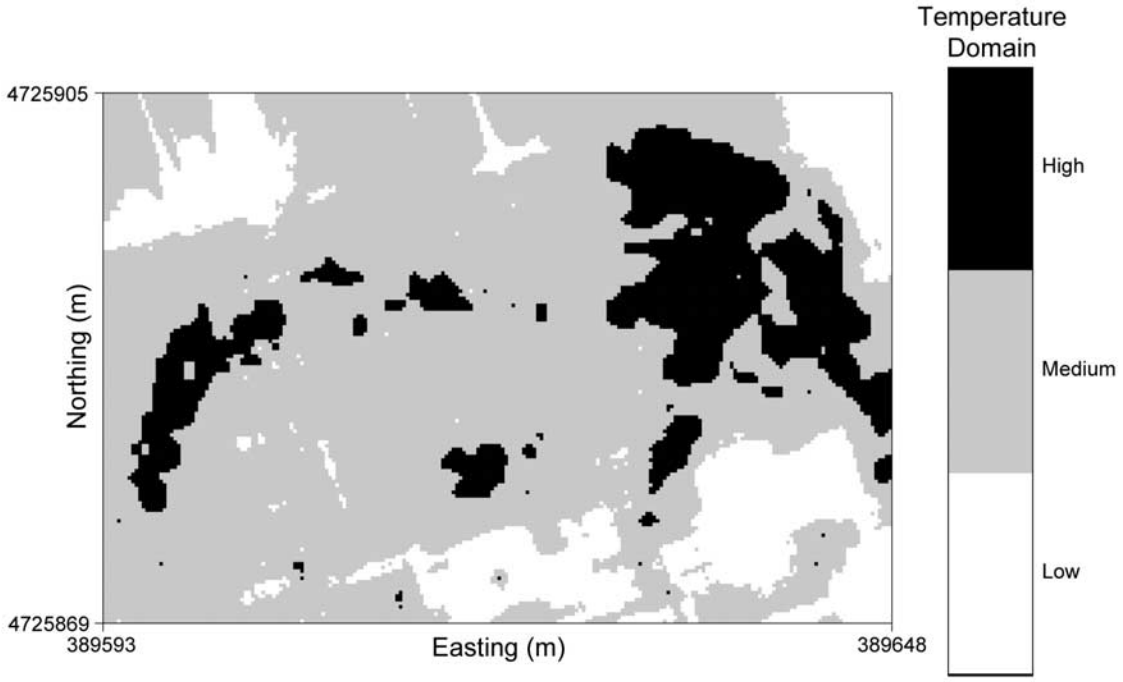

Figure 5. Temperature domains in the study site. Kriging was used to divide ground temperatures into three domains on the basis of the spatial statistics of the measured temperatures. The three domains, indicated in the figure, are low (measured temperatures less than 27.2°C), medium (temperatures between 27.2 and 58.1°C), and high temperatures (measured temperatures greater than 58.1°C).

that the practical ranges of the indicator variograms decreased symmetrically and continuously as p tended toward its bounding values of 0 and 1. Symmetric destructuration is a sufficient check for bivariate normality; although further checks for multivariate normality exist, it is common practice to assume multivariate normality if the data can be shown to posses bivariate normality [*Deutsch and Journel*, 1998].

[16] A variogram map based on the normal score temperatures was generated for each of the temperature domains; however, none of the maps suggested an apparent anisotropy in the structure of the continuous variable. As a result, isotropic experimental variograms of the normal score temperatures within each domain were computed, and model variograms were developed for the experimental variograms of each of the temperature domains. As might be expected, the model that best described the experimental variogram within each temperature domain differed between domains. A single exponential model was used to represent the low temperature domain; the medium temperature domain was modeled using nested spherical models, and the high temperature domain was adequately characterized by a single spherical model. A spherical model is defined mathematically as [*Deutsch and Journel*, 1998]:

$$\gamma(h) = \begin{cases} c \cdot \left[1.5\left(\frac{h}{a}\right) - 0.5\left(\frac{h}{a}\right)^3 \right], & h \le a \\ c, & h > a \end{cases}$$

where a is the actual range and c is the positive variance contribution; the parameters used to describe these models are given in Table 2. Figure 6 shows each experimental variogram and its corresponding model. The models were cross-validated, and the residuals were analyzed and checked against the criteria of *Kitanidis* [1997]. The validated normal score temperature variograms were input into the sequential Gaussian simulation routine, and 100 equally probable normal score temperature fields were simulated on a 55 × 36 m grid, at a resolution of 0.25 × 0.25 m/pixel for each domain. Individual realizations were based on the normal score variogram for the appropriate domain, and conditioned on any measured in-category data points and previously simulated points within the search radius. The simulated values for each category were averaged over the 100 equally probable simulations on a point-by-point basis ("E-type" estimates), and the pointwise averaged temperatures within each domain were truncated according to the domain geometry estimated in the IK procedure. Finally, E-type estimates for all three domains were superposed to obtain a representative simulated temperature field for the entire site; Figure 7 shows an image of the composite temperature field. Summary statistics of the simulated domains are compared

Table 2. Simulation Variogram Model Parameters, Isotropic Models

Domain	Structure	Nugget	Sill Contribution	Range
Low	exponential	0.20	0.80	9
Medium	spherical	0.30	0.35	6
	spherical		0.45	30
High	spherical	0.60	0.55	5

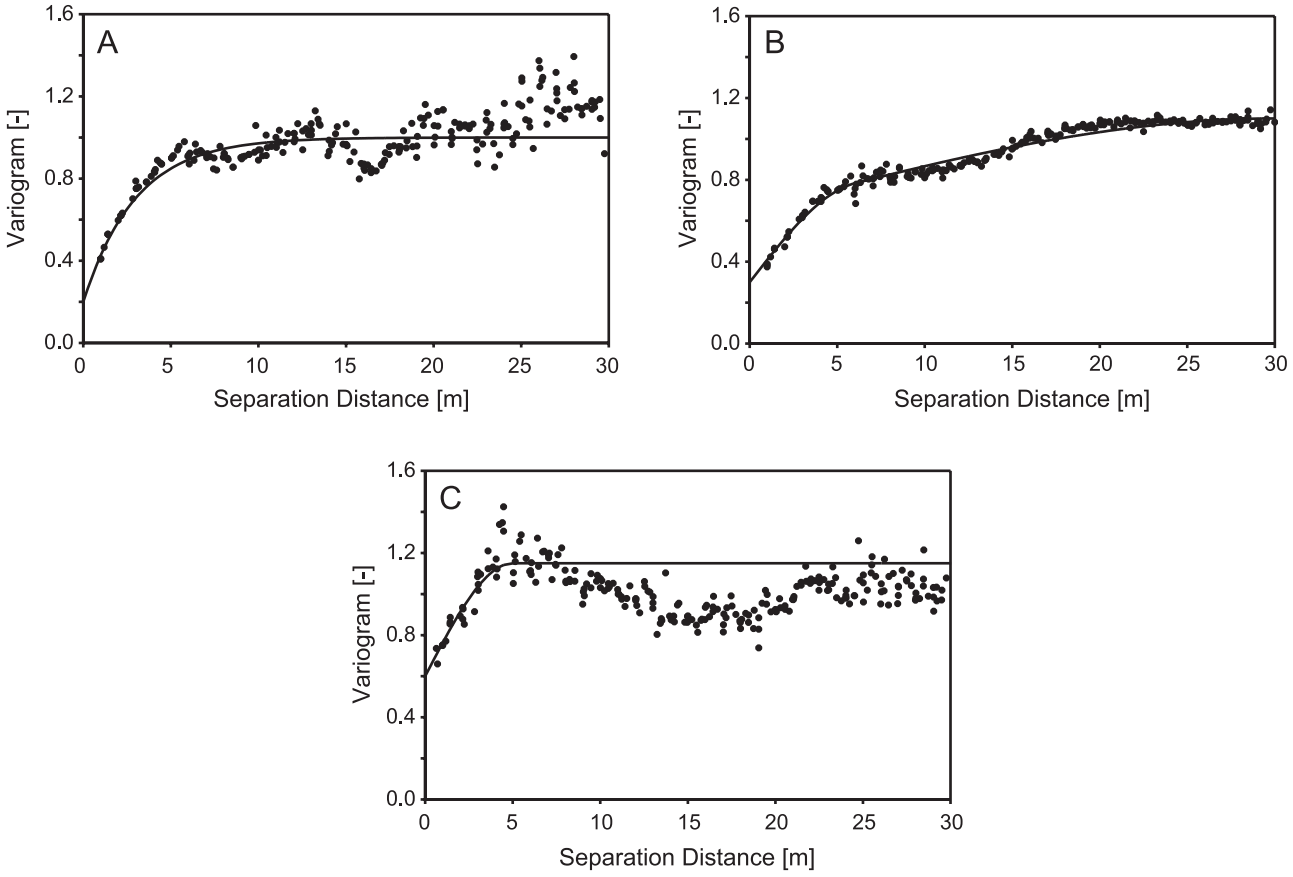

Figure 6. Continuous variable variograms. One isotropic variogram was used to represent the spatial structure of each temperature domain for in-category simulation of temperatures by sequential Gaussian simulation. Points represent experimental variogram values, while the solid lines are the model fits; parameters used in the models are presented in Table 2. (a) Low temperature domain variogram; (b) Medium temperature domain variogram; C. High temperature domain variogram.

to those of the sampled domains in Table 3; frequency histograms showing the distribution of temperatures within the simulated and sampled domains are presented in Figure 8.

5. Discussion and Interpretation

[17] *Curewitz and Karson* [1997] describe five specific structural settings in which hot springs are commonly found (Figure 9). On the basis of the spatial distribution of recurring patterns of hydrothermal spring expression, the five settings were given as: (1) Fault-tip lines. At the termination or tip of an isolated fault, a roughly circular breakdown region is expected to develop. Here, stress associated with fault propagation is concentrated at the tip, driving fracturing into the surrounding rock; (2) Fault interaction areas. Individual breakdown regions will merge when fault tip-lines are in proximity. In such interaction areas, shape and size of the modified breakdown region will depend on the specific geometry and kinematics of the individual faults; (3) Locked fault intersections. The junction of more than two faults with opposing slip vectors gives rise to a breakdown region in the intersection area that is controlled by the kinematic incompatibility of the opposing directions of slip; (4) Slipping fault intersections. The junction of faults with parallel or compatible slip vectors does not give rise to a significant breakdown region, since stress buildup is minimized at the fault intersection; and (5) Fault traces, where displacement on the fault may give rise to localized fracturing along the plane of slip. A sixth category, ''asystematic'' hot springs, was also defined to represent hydrothermal springs not obviously associated with any known fault. The investigators found that the structural settings that hosted hydrothermal springs varied somewhat between different tectonic settings, but among all tectonic settings the greatest percentage of hydrothermal activity was found in fault interaction areas, followed by (in order of decreasing prevalence) fault tip-lines, fault intersections, and fault trace settings [*Curewitz and Karson*, 1997]. As mentioned earlier, the motivation for the present study was, in part, to apply the methods developed in previous studies to a class of structural settings more widely distributed than fault trace hot springs, the category to which the Borax Lake Hot Springs belongs.

[18] Unfortunately, there is little information available to constrain the structural setting of the Mickey Hot Springs, other than the broad generalities discussed in the introductory section. The trace(s) of the controlling fault(s) are obscured by surficial alluvium, and descriptions of the faults differ somewhat between investigators. A number of factors, however, limit the possible structural settings that

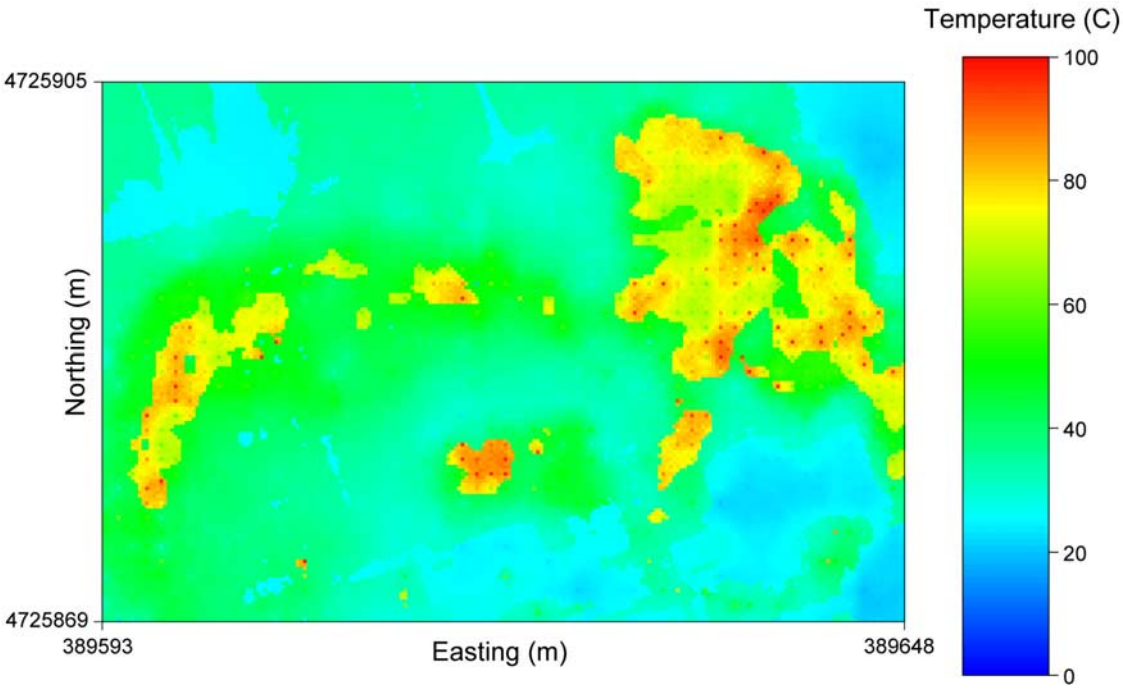

Figure 7. Composite temperature field for the Mickey Hot Springs study area. The composite temperature field shown represents the superposed results of 100 in-category sequential Gaussian simulations (E-type estimates), with values simulated at a spacing of 0.25 × 0.25 m. The simulation exactly honors the measured data points, which were collected on a spacing of 1 × 1 m.

could host the Mickey Hot Springs. As discussed by *Curewitz and Karson* [1997], the high average temperature of the springs (77.0°C for all the springs, and 86.9°C, with many of the spring temperatures pinned at the nominal boiling point, for the 35 springs in the area of the site described in the present study), pod-like geometry (as opposed to a linear distribution, as would be expected for a fault trace setting such as Borax Lake), and some evidence for spatial translation with time of the center of thermal activity all argue that the springs are located in a fault tip-line, fault interaction or locked intersection setting. The geometry of the breakdown region (region of fractured rock associated with stress concentration in and around the fault) controlling the distribution of springs at the Mickey site is strongly dependent on the mode of deformation, which in turn is determined by the magnitudes and orientations of stress components and the geometry of the fault system relative to the stress tensor. Considerable work has been done on understanding the geometry of fracturing associated with faulting; for example, in the process zone associated with a fault tip-line setting [e.g., *Cowie and Scholz*, 1992; *Scholz et al.*, 1993; *Vermilye and Scholz*, 1998], or in the step-over regions of strike-slip [*Connolly and Cosgrove*, 1999] and oblique-slip [*Crider*, 2001; *Crider and Pollard*, 1998] faults. It is possible that the thermal data presented here could be used in a detailed model of the site stress-field to determine the actual structural setting; however, such modeling is outside the scope of the present paper. We therefore limit the discussion below to descriptive and

Table 3. Summary Statistics for Model Domain and Sub-Domains

	Low		Medium		High		All	
	Sample	Simulated	Sample	Simulated	Sample	Simulated	Sample	Simulated
Mean	24.3	24.2	38.4	37.8	75.7	75.8	44.0	40.9
Standard error	0.12	0.02	0.27	0.04	0.66	0.08	0.50	0.09
Median	24.7	24.5	36.5	36.2	72.9	75.8	37.3	35.9
Mode	25.2	25.2	31.6	31.6	64.3	64.3	31.6	31.6
Standard deviation	2.03	1.48	8.32	5.64	12.16	5.81	19.65	16.25
Sample variance	4.11	2.18	69.16	31.76	147.85	33.81	386.04	264.11
Kurtosis	−0.26	0.34	−0.74	−0.25	−1.09	0.90	0.30	0.94
Skewness	−0.68	−0.87	0.60	0.70	0.45	0.41	1.09	1.35
Range	9.0	9.0	30.8	30.8	40.1	40.1	80.3	80.3
Minimum	18.2	18.2	27.3	27.3	58.4	58.4	18.2	18.2
Maximum	27.2	27.2	58.1	58.1	98.5	98.5	98.5	98.5
Count	288	6041	922	22211	340	4900	1550	33152

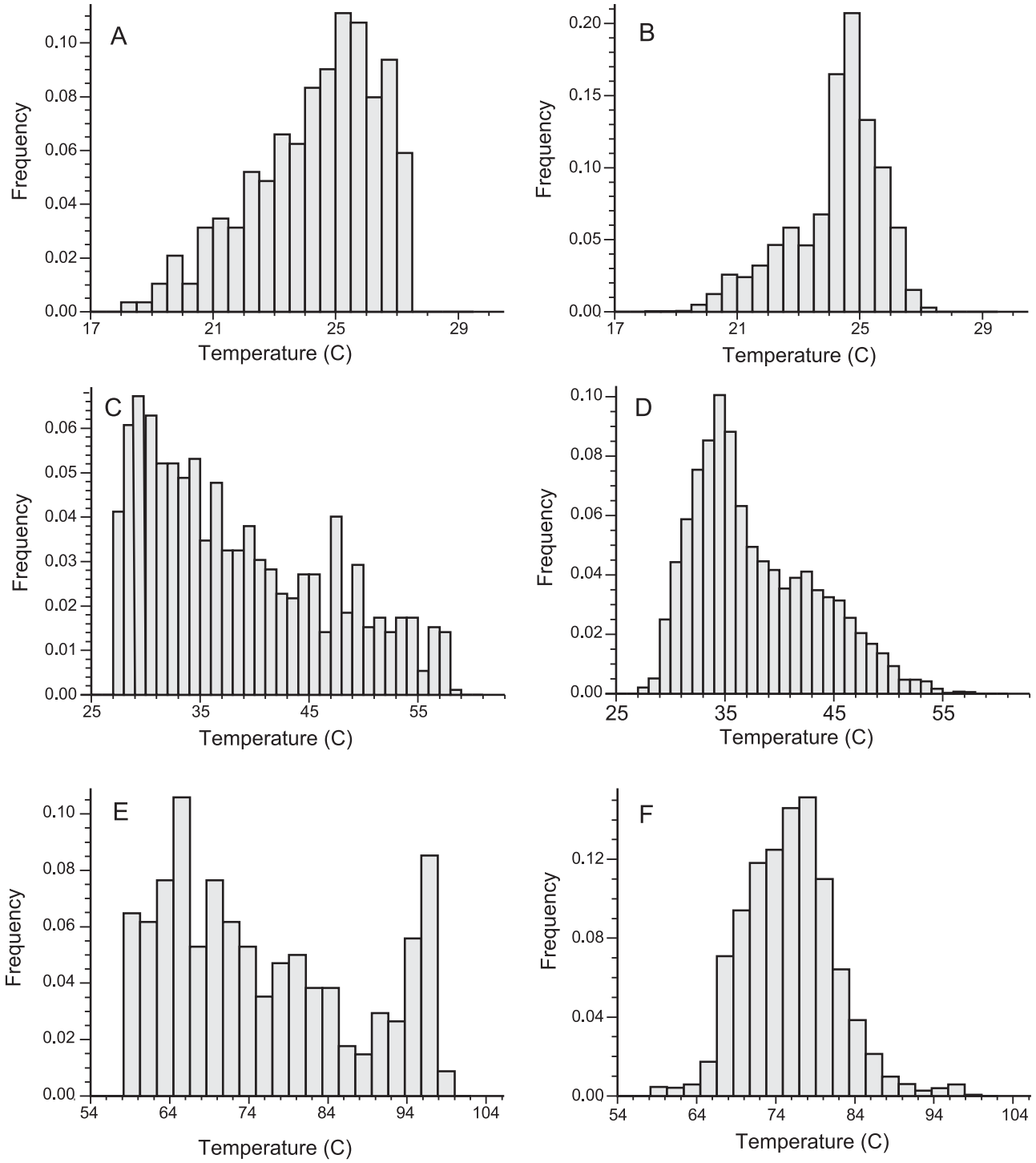

Figure 8. Frequency histograms for measured and simulated temperature data. (a) Measured temperature data from the low temperature domain; (b) Histogram for simulated temperatures in the low temperature domain; (c) Measured temperature data in the medium temperature domain; (d) Simulated temperature distribution in the medium temperature domain; (e) Measured data points for the high temperature domain; (f) Simulated temperatures in the high temperature domain.

conceptual comments regarding the controls placed on fluid flow by localized fracturing.

[19] Geostatistics is a family of primarily descriptive techniques of analysis, and therefore does not offer a physical explanation for the underlying drivers responsible for observed distributions of data. It is often possible, however, to attach physical significance to the spatial models developed. In the present case, probably the most valuable insights come from the indicator analysis, in which the measured temperature field was separated into three

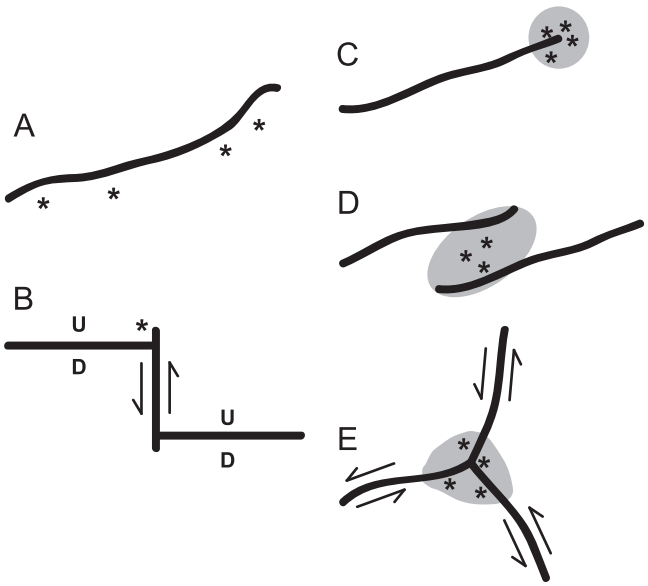

Figure 9. Structural settings of hot springs. Stars indicate the locations where hot springs are likely to develop in the given structural setting; breakdown regions are indicated by shading. (a) Fault trace (kinematically maintained); (b) Slipping fault intersection (kinematically maintained); (c) Fault tip (dynamically maintained); (d) Fault tip interaction area (dynamically maintained); (e) Locked fault intersection (dynamically maintained). Reprinted from *Curewitz and Karson* [1997] with permission from Elsevier.

domains (designated low, medium, and high temperature in a preceding section). This type of indicator analysis is designed to partition the domain into sub-areas that share an underlying generating process; that is, the spatial correlation structure within each sub-domain is internally homogeneous and arises as a result of physical factors that differ between the sub-domains. Because temperatures are roughly proportional to permeability, at least over a limited range [*Fairley et al.*, 2003; *Fairley and Hinds*, 2004; *Forster and Smith*, 1988; *Heffner and Fairley*, 2006], and because permeable pathways in hydrothermal systems are generally caused and maintained by fracturing, we postulate the high temperature areas in Figures 5 and 7 correspond to areas of more fracturing (or larger fractures), and represent the spatial pattern of the breakdown region. Two main zones or bands of high temperature are apparent in the figure; both

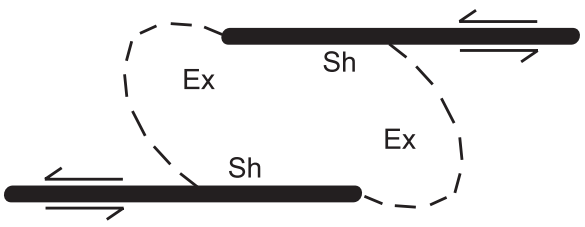

Figure 10. Expected stress distribution within a releasing step. Extensional fractures (Ex) should form in areas of tensile stress, or in areas of mixed tensile and shear stress. Shear fractures (Sh) should form in areas of transtension or shear stress. Reprinted from *Curewitz and Karson* [1997] with permission from Elsevier.

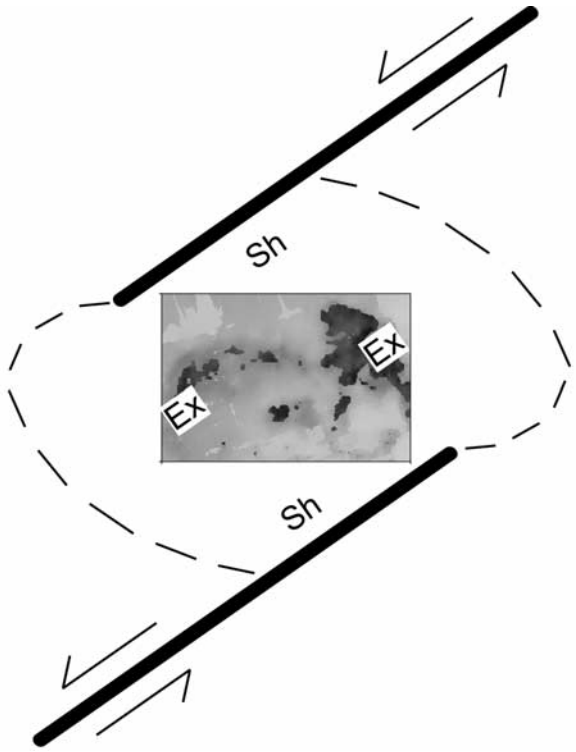

Figure 11. Conceptual setting at the Mickey Hot Springs area. Areas of high temperature, corresponding to high permeability, occur along the lateral margins where extensional fractures are likely to form.

zones are slightly curved, and they occur on opposite sides within the boundary of the study area. We propose these zones correspond to areas of opening-mode fractures; the directions of anisotropy indicated by the experimental variograms (30° and 120°, respectively, for the major and minor ranges of the high temperature domain) may be oriented parallel/normal to the trace of the fractures. This latter point will require verification by additional fieldwork, however, and separate analyses for two zones would be needed to detect any potential rotation of fracture orientations resulting from changes in the stress field. The medium temperature zones probably correspond to regions of compressional or shear fractures, which would be significantly less permeable than opening mode fractures, or to areas warmed by the diffusion of heat from the high temperature domain. Temperatures in the low temperature zones represent unperturbed or minimally perturbed conditions.

[20] The faults controlling Mickey Hot Springs, as mapped by J.S. Oldow [unpublished data, 2006; see Figure 3] are northeast-striking, left-stepping normal faults, oriented at an angle of roughly 35° to the dominant direction of extension, which would result in a significant component of left-lateral slip, in addition to the dip-slip. Left-oblique slip on a left-stepping fault will produce a zone of extension in the ramp area between the segments (i.e., a releasing step), as shown schematically in Figure 10. Figure 11 shows a conceptual diagram illustrating the study area in such a situation, assuming the orientation of the step-over as mapped by J.S. Oldow and the simulated temperature field from Figure 7. For this scenario, *Crider*'s [2001]

modeling of oblique slip is probably the most relevant, although elements of *Connolly and Cosgrove*'s [1999] model for pure strike-slip also offer insights into the distribution of fracturing in the study area (e.g., compare the location and curvature of the high temperature regions of Figure 7 of this study with the narrow bands of extensional fracturing that connect the fault segments in Figures 3c and 3d of *Connolly and Cosgrove* [1999]). On the basis of the conceptual model of Figure 11 and the numerical results of *Crider* [2001], the ratio of overlap to spacing between the fault segments would be estimated to be on the order of 1:1 or 1.2:1. Furthermore, as *Crider* [2001] pointed out, when the sense of step and sense of oblique slip are the same (i.e., a left-step with left-oblique slip, as in the present instance), echelon fault segments are most likely to breach on the low part of the relay ramp between the segments, which would explain the large, better-developed area of high temperatures in the northeast part of the study domain (Figure 7); thus, the observed distribution of temperatures at Mickey Hot Springs could be viewed as a possible snapshot of a ramp-breach in progress.

[21] Interpretations other than that offered in Figure 11 are also possible; for example, the springs may be located in a fault tip-line setting. In the case of fault tips, the breakdown area/process zone would be expected to be roughly circular in shape, with a radius that scales as 0.01L to 0.1L, where L is the length of the fault [*Cowie and Scholz*, 1992; *Scholz et al.*, 1993; *Vermilye and Scholz*, 1998], offering the possibility of constraining the length of the fault with the help of the information presented in Figures 5 and 7. Although the system geometry cannot be determined uniquely at the level of analysis presented here, we believe the ability to delineate the probable extent of fracturing associated with the controlling fault(s), when combined with detailed mapping of site-specific features, offers the potential to gain more information about the site than would be possible without the temperature data.

6. Conclusions

[22] In this study we have presented a geostatistical analysis of temperature distributions arising from the discharge of hydrothermal fluids at Mickey Hot Springs in the Alvord Basin of southeast Oregon. Indicator transforms and variogram modeling were used to treat major heterogeneities, separating the study site into domains of distinct characteristics, and the geometries of the resulting domains were modeled using indicator kriging. Within each domain, sequential Gaussian simulation was used to generate 100 equally probable temperature field realizations, based on 1550 data points measured at the land surface over the study area. The in-domain simulations, which were conditioned to match the measured data points, were averaged on a point-by-point basis, then truncated by domain and combined to form a composite image of shallow subsurface temperatures in the study area (Figure 7).

[23] Because temperatures are roughly proportional to permeability, at least over a limited range [*Fairley et al.*, 2003; *Fairley and Hinds*, 2004; *Forster and Smith*, 1988; *Heffner and Fairley*, 2006], and because permeable pathways in hydrothermal systems are generally caused and maintained by fracturing, we postulate the high temperature areas at Mickey Hot Springs (Figure 7) correspond to areas of more fracturing (or larger fractures), and represent the pattern of the breakdown region associated with the fault(s) controlling the observed hydrothermal discharge. Although the available data are insufficient to uniquely determine the structural setting of the springs the observed distribution of temperatures is consistent with the location of the study area in a fault tip-line region or in a releasing step within an obliquely slipping fault interaction area.

[24] Predicting the transport of energy and fluids in fault-controlled settings is important for a number of disciplines; previous efforts to model the controls placed on fluid flow in faulted environments have been motivated, for example, by applications to hydrocarbon migration and trapping [e.g., *Crider*, 2001; *Crider and Pollard*, 1998] or to ore emplacement [e.g., *Connolly and Cosgrove*, 1999; *Cox and Knackstedt*, 1999]. In this paper, we have tried to point out that observable quantities such as the presence and spatial distribution of springs or the spatial distribution of temperatures in hydrothermal outflow zones can feed back into an understanding of the geometry of the controlling faults, the way in which the local stress field is perturbed by faulting, and the extent and orientation of fracturing associated with deformation. Although the information presented is primarily descriptive of the thermal-hydrologic characteristics of the site, we believe the potential exists to extract additional detail regarding the mechanical and thermal-mechanical conditions through the application of more sophisticated techniques. At a minimum, the study illustrates the importance of incorporating hydrologic and thermal information whenever possible in characterizing fault zones, and suggests that thermal-hydrologic data, collected in a fashion similar to that described above, may constitute an additional source of information for the study of fault-controlled deformation.

[25] **Acknowledgments.** The authors would like to thank J.S. Oldow for allowing his map of faults in the Mickey Basin to be used in the present study, and the field team responsible for collecting the data used in this study: A. Colter, L. Garringer, J. Hinds, K. Link, and K. Nicholson. The original manuscript was strengthened and greatly improved as a result of review comments by N. Davatzes and R. Lunn. Additional thanks are due to J. Hinds for assistance with maps and figures for the manuscript. Fieldwork for this study was supported by the National Science Foundation under award EAR-0511061.

References

Barton, C., M. D. Zoback, and D. Moos (1995), Fluid flow along potentially active faults in crystalline rocks, *Geology*, *23*, 683–686.

Bishop, B. P., and D. K. Bird (1987), Variation in sericite compositions from fracture zones within the Coso hot springs geothermal system, *Geochim. Cosmochim. Acta*, *51*, 1245–1256.

Brown, D. E., and N. V. Peterson (1980), Preliminary geology and geothermal resource potential of the Alvord Desert area, Oregon, *Oregon Department of Geology and Mineral Industries Open-File Report 0-80-10*, 57 pp.

Caine, J. S., J. P. Evans, and C. B. Forester (1996), Fault zone architecture and permeability structure, *Geology*, *24*, 1025–1028.

Catton, I. (1985), Natural convection heat transfer in porous media, in *Natural Convection, Fundamentals and Applications*, edited by S. Kakaç, W. Aung, and R. Viskanta, pp. 514–547, Hemisphere Publishing Corporation, New York.

Cheng, P. (1985), Natural convection in a porous medium: External flows, in *Natural Convection, Fundamentals and Applications*, edited by S. Kakaç, W. Aung, and R. Viskanta, pp. 475–513, Hemisphere Publishing Corporation, New York.

Chester, F. M., and J. M. Logan (1986), Implications for mechanical properties of brittle faults from observations of the Punchbowl fault zone, California, *Pure Appl. Geophys.*, *124*, 79–106.

Cleary, J. G. (1974), Geothermal investigation of the Alvord Valley, southeast Oregon, M.S. thesis, University of Montana.
Connolly, P. T., and J. W. Cosgrove (1999), Prediction of static and dynamic fluid pathways within and around dilational jogs, in *Fractures, Fluid Flow and Mineralization*, edited by K. J. W. McCaffrey, L. Lonergan, and J. J. Wilkinson, pp. 105–121, Geological Society, London, Special Publications 155.
Cowie, P. A., and C. H. Scholz (1992), Growth of faults by accumulation of seismic slip, *J. Geophys. Res.*, *97*(7), 11,085–11,095.
Cox, S. F., and M. A. Knackstedt (1999), Ore genesis in fracture-controlled hydrothermal systems: Percolation theory approaches, in *PACRIM '99 Congress, 10–13 October 1999, Bali, Indonesia*, pp. 639–642.
Cressie, N. (1985), Fitting variogram models by weighted least squares, *Math. Geol.*, *17*, 563–586.
Crider, J. G. (2001), Oblique slip and the geometry of normal-fault linkage: Mechanics and a case study from the basin and range in Oregon, *J. Struct. Geol.*, *23*, 1997–2009.
Crider, J. G., and D. D. Pollard (1998), Fault linkage: Three-dimensional mechanical interaction between echelon normal faults, *J. Geophys. Res.*, *103*(B10), 24,373–24,391.
Cummings, M. L., A. M. St. John, and N. C. Sturchio (1993), Hydrogeochemical characterization of the Alvord Basin geothermal area, Harney County, Oregon, USA, in *Proceedings of the 15th New Zealand Geothermal Workshop*, *Auckland*, pp. 119–124.
Curewitz, D., and J. A. Karson (1997), Structural settings of hydrothermal outflow: Fracture permeability maintained by fault propagation and interaction, *J. Volcanol. Geotherm. Res.*, *79*, 149–168.
Davatzes, N. C., and S. Hickman (2005), Controls on fault-hosted fluid flow: Preliminary results from the Coso geothermal field, CA, *Trans. Geotherm. Resour. Counc.*, *29*, 343–348.
Davatzes, N. C., P. Eichhubl, and A. Aydin (2005), Structural evolution of faults in sandstone by multiple deformation mechanisms: Moab fault, SE Utah, *Geol. Soc. Am. Bull.*, *117*, 135–148, doi:10.1130/B25473.1.
Davis, B. M. (1987), Uses and abuses of cross-validation in geostatistics, *Math. Geol.*, *19*, 241–248.
Deutsch, C. V., and A. G. Journel (1998), *GSLIB: Geostatistical Library and User's Guide*, 369 pp., Oxford University Press, New York.
Eaton, T. T. (2006), On the importance of geological heterogeneity for flow simulation, *Sediment. Geol.*, *184*, 187–201.
Elders, W. A., D. K. Bird, A. E. Williams, and P. Schiffman (1984), Hydrothermal flow regime and magmatic heat source of the Cerro Prieto geothermal system, Baja California, Mexico, *Geothermics*, *12*, 27–47.
Fairley, J. P., and J. J. Hinds (2004), Rapid transport pathways for geothermal fluids in an active Great Basin fault zone, *Geology*, *32*, 825–828.
Fairley, J. P., J. Heffner, and J. J. Hinds (2003), Geostatistical evaluation of permeability in an active fault zone, *Geophys. Res. Lett.*, *30*(18), 1962, doi:10.1029/2003GL018064.
Forster, C., and L. Smith (1988), Groundwater flow systems in mountainous terrain 2. Controlling factors, *Water Resour. Res.*, *24*(7), 1011–1023.
Fuller, R. E. (1931), The geomorphology and volcanic sequence of Steens Mountain in southeast Oregon, *Univ. Washington Publ. Geol.*, *3*, 1–130.
Goovaerts, P. (1997), *Geostatistics for Natural Resources Evaluation*, 483 pp., Oxford University Press, New York.
Goovaerts, P., R. Webster, and J. P. Dubois (1997), Assessing the risk of soil contamination in the Swiss Jura using indicator geostatistics, *Environ. Ecol. Stat.*, *4*, 31–48.
Heffner, J., and J. P. Fairley (2006), Using surface characteristics to infer the permeability structure of an active fault zone, *Sediment. Geol.*, *184*, 255–265.
Hickman, S., M. D. Zoback, and R. Benoit (1998), Tectonic controls on fault-zone permeability in a geothermal reservoir at Dixie Valley, Nevada, in *SPE/ISRM Rock Mechanics in Petroleum Engineering Proceedings, 8–10 July, 1998, Trondheim, Norway*, pp. 79–86.
Hook, R. (1981), The volcanic stratigraphy of the Mickey Hot Springs area, Harney County, Oregon, M.S. thesis, Oregon State University.
Isaaks, E. H., and R. M. Srivastava (1989), *An Introduction to Applied Geostatistics*, 561 pp., Oxford University Press, New York.
Journel, A. G., and F. G. Alabert (1990), New method for reservoir mapping, *J. Petrol.*, 212–218, February.
Journel, A. G., and E. H. Isaaks (1984), Conditional indicator simulation: Application to a Saskatchewan uranium deposit, *Math. Geol.*, *16*, 685–718.
Kitanidis, P. K. (1997), *Introduction to Geostatistics: Applications in Hydrogeology*, 249 pp., Cambridge University Press, New York.
Koltermann, C. E., and S. M. Gorelick (1996), Heterogeneity in sedimentary deposits: A review of structure-imitating, process-imitating, and descriptive approaches, *Water Resour. Res.*, *32*(9), 2617–2658.
Koski, A. K., and S. A. Wood (2004), The geochemistry of geothermal waters in the Alvord Basin, southeastern Oregon, in *Proceedings of the 11th International Symposium on Water-Rock Interaction, Energy and Environment, Saratoga Springs, New York*, Lawrence Livermore National Laboratory, Livermore, California.
Lawrence, R. D. (1976), Strike-slip faulting terminates the basin and range province in Oregon, *Geol. Soc. Am. Bull.*, *87*, 846–850.
Lindberg, D. N. (1999), A synopsis of Late Pleistocene shorelines and faulting, Tule Springs Rims to Mickey Basin, Alvord Desert, Harney County, Oregon, in *Quaternary Geology of the Northern Quinn River and Alvord Valleys, Southeastern Oregon: Friends of the Pleistocene Field Trip Guide, September 24–26, 1999*, pp. 1–13.
Micklethwaite, S., and S. F. Cox (2004), Fault-segment rupture, aftershock zone fluid flow, and mineralization, *Geology*, *32*, 813–816.
Minor, S. A., J. J. Rytuba, C. A. Goeldner, and K. J. Tegtmeyer (1987), Geologic map of the Alvord Hot Springs Quadrangle, Harney County, Oregon, *U.S. Geol. Surv.*, *Miscellaneous Field Studies Map MF-1916*.
Norton, D., and R. Knapp (1977), Transport phenomena in hydrothermal systems: The nature of porosity, *Am. J. Science*, *277*, 913–936.
Pezzopane, S. K., and R. J. Weldon (1993), Tectonic role of active faulting in Central Oregon, *Tectonics*, *12*, 1140–1169.
Rubin, Y. (2003), *Applied Stochastic Hydrogeology*, 391 pp., Oxford University Press, New York.
Rytuba, J. J., D. B. Vander Meulen, T. L. Vercoutere, and S. A. Minor (1982), Reconnaissance geologic map of the Borax Lake Quadrangle, Harney County, Oregon, *U.S. Geol. Surv.*, *Open File Report 82-1126*.
Scholz, C. H., N. H. Dawers, J.-Z. Yu, and M. H. Anders (1993), Fault growth and fault scaling laws: Preliminary results, *J. Geophys. Res.*, *98*(B12), 21,951–21,961.
Sherrod, D. R., S. A. Minor, and T. L. Vercoutere (1989), Geologic map of the Sheepshead Mountains, Harney and Malheur County, Oregon, *U.S. Geol. Surv.*, *Miscellaneous Field Studies Map MF-2079*.
Sibson, R. H. (1987), Earthquake rupturing as a mineralizing agent in hydrothermal systems, *Geology*, *15*, 701–704.
Suro-Perez, V., and A. G. Journel (1990), Stochastic simulation of lithofacies: An improved sequential indicator approach, in *2nd European Conference on the Mathematics of Oil Recovery*, Paris, pp. 3–10.
Vermilye, J. M., and C. H. Scholz (1998), The process zone: A microstructural view of fault growth, *J. Geophys. Res.*, *103*(B6), 12,223–12,237.
Walker, G. W., and N. S. MacLeod (1991), Geologic map of Oregon, *U.S. Geol. Surv.*, *Special Geologic Map*, scale 1:500,000.
Walker, G. W., and C. A. Repenning (1965), Reconnaissance meologic map of the Adel Quadrangle, Lake, Harney, and Malheur Counties, Oregon, in *U.S. Geol. Surv.*, Miscellaneous Geologic Investigations Map I-446.
Weldon, R. J., D. K. Fletcher, E. M. Weldon, and K. M. Scharer (2003), An update of Quaternary faults of central and eastern Oregon, *U.S. Geol. Surv.*, *Open-File Report 02-301*.
Williams, H., and R. R. Compton (1953), Quicksilver deposits of Steens Mountain and Pueblo Mountains, southeast Oregon, *U.S. Geological Survey Bulletin 995-B*, 19–77.
Wong, K., and A. Dybbs (1976), An experimental study of thermal equilibrium in liquid saturated porous media, *Int. J. Heat Mass Transfer*, *18*, 234–235.

T. R. Anderson, Environmental Science Program, University of Idaho, Moscow, ID 83844-3006, USA.
J. P. Fairley, Department of Geological Sciences, University of Idaho, Moscow, ID 83844-3022, USA. (jfairley@uidaho.edu)